https://doi.org/10.1038/s44182-025-00053-0

Designing novel carangiform fish robots with undulating hair clip mechanisms

Check for updates

Zechen Xiong[1,2] ✉, Liqi Chen[2], Sarah Li Wilkinson[2], Md Raf E. Ul Shougat[1,3] & Hod Lipson[2]

Bi- and multistable mechanisms have gained significant attention in the field of soft and compliant robotics due to their distinctive mechanical and dynamic properties, which enable complex motion, adaptability, and energy-efficient actuation for various applications. This study investigates the Hair Clip Mechanism (HCM), defined as a kinked ribbon with its two extremities pinned together, analogous to a snap hair clip. While previous studies have explored similar concepts, they have not specifically investigated the snapping behavior of hair clip-like mechanisms as robotic actuators, leaving a critical gap in the understanding and application of this unique bistable structure. This paper systematically analyzes the static and dynamic properties of a generalized HCM, validates the theoretical models through experimentation, and demonstrates its application in the design of two distinct versions of carangiform fish robots. The first, a tethered pneumatic fish robot, achieves a swimming speed of 1.40 body lengths per second (BL/s) or 26.54 cm/s, approximately twice the velocity of a conventionally designed counterpart. The second, an untethered motor-driven HCM-based fish robot, attains a speed of 2.03 BL/s or 42.6 cm/s, thrust of 245.66 mN, cost of transport (CoT) of 5.14, energy efficiency of 3.89%, and thrust-to-power ratio of 79.46 mN/W at 3 Hz undulation. These metrics position it among the fastest soft robotic swimmers reported. Notably, its performance is 40% (in BL/s) higher than that of the previously documented record-holding design. These findings highlight the potential of HCM-based structures to enhance the adaptability and performance of soft robotic systems, paving the way for innovative applications in bio-inspired locomotion and compliant mechanism design.

Compliant mechanisms with bi- or multi-stability have gained significant attention due to their ability to undergo rapid, strong, and repetitive deformations[1–9]. Bistable mechanisms, in particular, enable elastic energy to accumulate through slow, continuous actuation with low forces and release it rapidly upon reaching a critical actuation threshold. This principle, akin to latch-mediated spring actuation (LaMSA) systems[10], is widely observed in nature. Examples include the ballistic seed dispersal of *Impatiens* and squirting cucumber after prestressing their seedpods[11], the pollen dispersal of trigger plants[12], the rapid leave closure of the iconic Venus flytrap[13], the fast snap-through of hummingbird beaks[14], the ballistic jaw propulsion in trap-jaw ants[15], and the bistable folding and unfolding of earwigs[16]. In robotics, bistable mechanisms are particularly advantageous for enhancing the speed and force of soft robots, since they often struggle with slow actuation and limited manipulation forces.

Soft robots, typically constructed from materials with moduli ranging from 10^4–10^9 Pa[17,18], are valued for their safety, versatility, and biocompatibility. However, their intrinsic material properties often limit their actuation speed. Pneumatic actuation is a common solution, though it poses challenges for untethered operation. Various strategies have been explored to address the challenges of speed and untethering of soft robotics, such as explosive actuators for high-speed jumping robots[19–23], optimized pneumatic networks for increased reaction speed[24], CO_2-based untethered propulsion systems[25], and direct drive of a continuum body[26]. Additionally, researchers have leveraged snap-through instability and bistable mechanisms to achieve rapid movement and enhanced locomotion in soft robotic designs. Examples include bistable galloping robots[27], magnetic elastomer robots[28], and bistable fishtail designs that improve energy efficiency[29].

Inspired by these advancements, our work explores the use of hair-clip-inspired bistable mechanisms (HCMs) for soft robotic fish propulsion. HCMs, constructed from semi-rigid ribbon materials under in-plane prestressing, offer a promising approach to enhancing both speed and untethered mobility. These mechanisms exhibit compliant deformation with an infinite degree of freedom, making them suitable for

[1]Ingram School of Engineering, Texas State University, San Marcos, TX, USA. [2]Department of Mechanical Engineering, Columbia University, New York, NY, USA. [3]Department of Mechanical Engineering, Kennesaw State University, Marietta, GA, USA. ✉e-mail: uji21@txstate.edu

integration into soft robotic systems. Despite their growing popularity, theoretical modeling and closed-form solutions for HCMs remain challenging due to the large deflections involved in their deformation and actuation phases. This paper introduces an approximate calculation method for HCMs to establish fundamental design principles for HCM-based robotic applications, validated through finite-element simulations and experimental testing.

Structurally, HCMs consist of kinked ribbons or thin-walled beams with their extremities pinned together, forming a core region (denoted as L_1 in Fig. 1A) that facilitates actuation and bistable triggering. Upon activation, stored elastic energy propagates in the form of an undulating wave, resembling the carangiform swimming pattern observed in fish. Building upon this analogy, we developed two fish robots utilizing HCMs to explore their potential for novel aquatic locomotion. We fabricated a pneumatic HCM fish robot and compared its performance against a traditionally actuated swimmer. Additionally, a servo-driven HCM fish prototype was constructed and tested in a natural lake environment. A video showcasing the operation principle and the experiments of the untethered HCM fish robot is provided (Fig. 2).

Methods

The Theory of HCM bistability

Compressed slender elements like ribbons, beams, and rods have a strong tendency to buckle[30,31]. The lateral-torsional buckling of a typical HCM is first triggered when the HCM is prestressed and riveted, as in Fig. 1A–D and Fig. 3, in which L_1 is the half-length of the core section of the HCM ribbon measured by the midline and L_2 is the length of the props measured by the midline; a non-dimensional shape factor $\gamma_s = L_2 / L_1$ is defined for the derivation of unit-free principles; angle θ is the twist at the kinked corner of the HCM, which is another non-dimensional shape factor than γ_s; h is the ribbon width; t is the ribbon thickness. The lateral symmetry of the HCM ribbons is used for simplicity so that the mathematical derivations can be conducted on a half-HCM. Compressed slender elements like ribbons, beams, and rods have a strong tendency to buckle[30,31]. The lateral-torsional buckling of a typical HCM is first triggered when the HCM is prestressed and riveted, as in Fig. 1A–D and Fig. 3, in which L_1 is the half-length of the core section of the HCM ribbon measured by the midline and L_2 is the length of the props measured by the midline; a non-dimensional shape factor $\gamma_s = L_2 / L_1$ is defined for the derivation of unit-free principles; angle θ

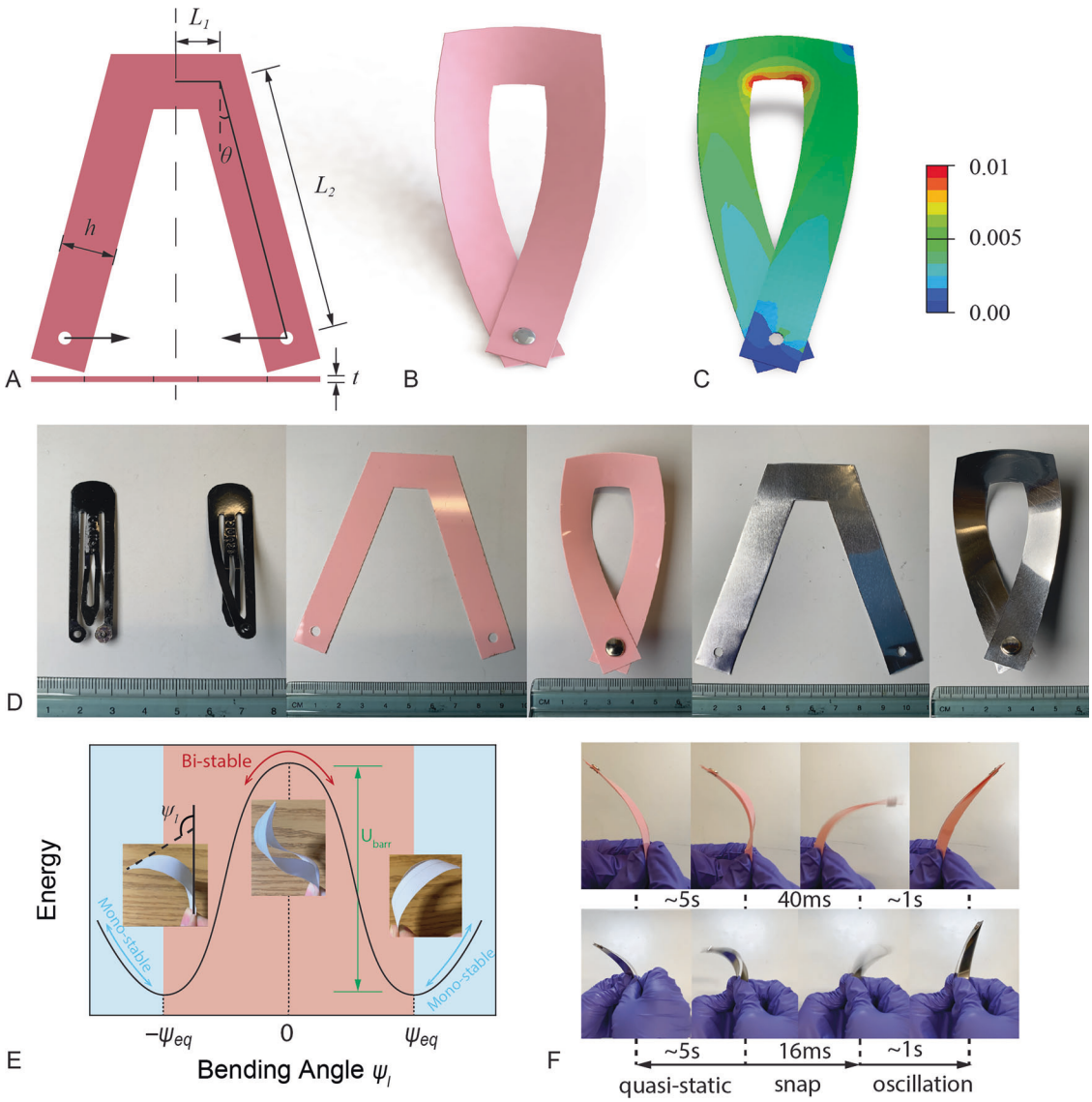


Fig. 1 | Design and working principles of hair clip mechanisms (HCMs). A The geometry of the HCM ribbon before assembly. Dimensionless shape factors $\theta = 10^\circ$ and $\gamma_s = L_2 / L_1 = 6$; other parameters $h/L_1 = 15$ mm/12.5 mm and $t/L_1 = 0.381$ mm/12.5 mm. **B**, **C** Assembled configuration and contour of maximum principal strain from FE simulation, respectively. **D** HCMs made of steel and plastic sheets. **E** Energy profile and configuration transition of a snapping HCM. **F** Time series of snapping plastic and steel HCMs under a high-speed camera.

is the twist at the kinked corner of the HCM, which is another non-dimensional shape factor than γ_s; h is the ribbon width; t is the ribbon thickness. The lateral symmetry of the HCM ribbons is used for simplicity so that the mathematical derivations can be conducted on a half-HCM.

Variable definitions are shown in Fig. 3. The displacements u, v, and φ are measured on centroid C of an arbitrary section mn along x, y, and z axes (undeformed coordinate system of the HCM, Fig. 3A), respectively, with signs following the directions of axes and right-hand rule. Here, a "kinked-to-straight" assumption is used so that the z coordinate can conveniently denote the arc length of the half ribbon to reduce the model complexity. This assumption is based on the fact that the bending moments on the two sides of the kind are conserved, and usually, bending moments contribute to a major part of the beam deflections. The ξ, η, and ζ axes (deformed coordinate system) are drawn through the deformed centroid C' of the section mn, with positive directions coinciding with the principal axes of the deformed configuration.

Another assumption we need to obtain a solvable equation group for an Euler-Bernoulli beam is the small deflection assumption, which states that the beam curvature

$$\kappa \overset{def}{=} \frac{Y''}{\left(1+Y'^2\right)^{3/2}} \approx Y'' \tag{1}$$

Thus, the mathematical model of the assembly process can be given by the following equations[32]:

$$EI_\xi \frac{d^2v}{dz^2} + P(l-z) = 0 \tag{2}$$

$$EI_\eta \frac{d^2u}{dz^2} + P\varphi(l-z) = 0 \tag{3}$$

$$-C\frac{d\varphi}{dz} + P(l-z)\frac{du}{dz} - P(u_1-u) = 0 \tag{4}$$

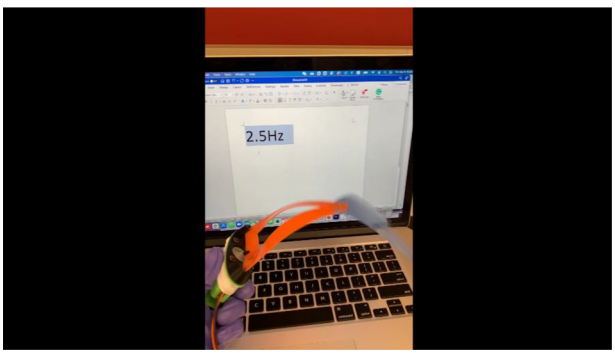


Fig. 2 | The operation principle and experiments of the untethered HCM fish robot.

in which I_η and I_ξ denote the second axial moment of area for axes ξ and η, $EI_i = E \times (\text{width}_i) \times (\text{height}_i)^3/12$ is the bending stiffness of the beam along the i axis (Fig. 3), $l = L_1 + L_2$ is the half-length of the strip, $C = GJ = hb^3G/3$ is the torsional rigidity of the thin rectangular section mn if only $h > 10t$, u_1 is the horizontal deflection at $z = l$, $G = E/2/(1-v)$ is the shear modulus, and v the Poisson ratio. Differentiating Eq. (4) w.r.t z and plugging in Eq. (3) yields

$$C\frac{d^2\varphi}{dz^2} + \frac{P^2(l-z)^2}{EI_\eta}\varphi = 0 \tag{5}$$

The general solution of Eq. (5) can be analytically given as

$$\varphi(s) = \sqrt{s}\left[A_1 J_{1/4}\left(\frac{\beta_1}{2}s^2\right) + A_2 J_{-1/4}\left(\frac{\beta_1}{2}s^2\right)\right] \tag{6}$$

where $s = l - z$, $J_{1/4}$ and $J_{-1/4}$ represent Bessel functions of the first kind of order 1/4 and −1/4, respectively, and the notation

$$\beta_1 = \sqrt{\frac{P^2}{EI_\eta C}}. \tag{7}$$

Due to the symmetry of the ribbon and the small deflection assumption, integration constant $A_2 = 0$ can be inferred from the boundary condition

$$\varphi|_{s=0} = 0. \tag{8}$$

Thus, the general solution of Eqs. (2)–(4) can be described by

$$\varphi(s) = \sqrt{s}A_1 J_{1/4}\left(\frac{\beta_1}{2}s^2\right) \tag{9}$$

where A_1 is a non-zero integration constant. Equation (9) indicates that the ribbon will buckle in a way that the twist φ(s) follows a Bessel function of order 1/4. Another boundary condition of the beam can be described as

$$\varphi|_{s=l} = 0 \tag{10}$$

since the two extremities are hinged together. Due to the lack of lateral support on the beams and the non-zero feature of A_1, the lowest root of the Bessel function $J_{1/4}$ should be used when combining Eqs. (9) and (10), which dictates that the variable

$$\frac{\beta_1}{2}l^2 = 2.7809 \tag{11}$$

Plugging in Eq. (4), the critical load of the lateral-torsional buckling is

$$P_{cr} = \frac{5.5618}{l^2}\cdot\sqrt{EI_\eta C} \tag{12}$$

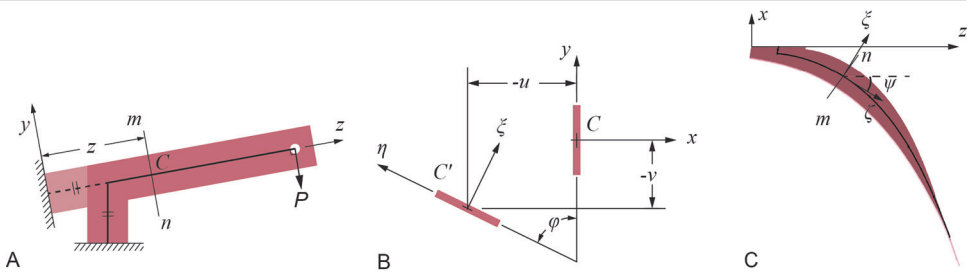


Fig. 3 | Mathematical model of the hair clip mechanism (HCM). A The kinked-to-straight assumption and the undeformed half HCM in the y-z plane. **B** Displacements of the arbitrary section mn in the x-y plane. **C** Deformed shape of the HCM in the x-z plane.

The post-buckling load is usually assumed to equal the critical load. However, because the "kinked-to-straight" assumption releases the constraint of the model, one more equation is needed for the particular solution, i.e., for getting the values of A_1 and then φ. Usually, the energy conservation law is used, which can be expressed as the fact that the total elastic strain energy of the structure must equal the work done by the external critical load P_{cr}. Ignoring the membrane strain energy, we have

$$\begin{aligned} U &= \tfrac{1}{2}\int_0^l \left[\frac{M_\eta^{\,2}}{EI_\eta} + GJ\left(\frac{d\varphi}{dz}\right)^2\right] dz \\ &= \tfrac{1}{2}\int_0^l \left[P_{cr}^{\,2}(l-z)^2\sin^2\varphi/EI_\eta + GJ\left(\frac{d\varphi}{dz}\right)^2\right] dz \end{aligned} \tag{13}$$

in which U is the total elastic energy, M_η is the moment on the beam along axis η. On the other hand, the total external work done by P_{cr} is

$$T = P_{cr}\cdot L_2\left(\sin^{-1}\frac{1}{\gamma_s} + \theta\right) \tag{14}$$

where $\gamma_s = L_2 / L_1$ and θ are the two non-dimensional shape factors of the HCM. By plugging in

$$U = T \tag{15}$$

we can solve for the value of A_1, and then the analytical expression of φ from Eq. (9). Finally, by plugging Eq. (9) into Eq. (3), the out-of-plane bending angle ψ of the section mn is

$$\begin{aligned} \psi(z) \approx \tfrac{du}{dz} &= -\tfrac{P_{cr}}{EI_\eta}\int_0^z \varphi(l-\zeta)\cdot(l-\zeta)\,d\zeta + C_0 \\ &= -\tfrac{P_{cr}}{EI_\eta}\int_0^z \sqrt{l-\zeta}A_1 J_{1/4}\left(\frac{\beta_1}{2}(l-\zeta)^2\right)\cdot(l-\zeta)\,d\zeta + C_0 \end{aligned} \tag{16}$$

in which the integral constant C_0 is zero by plugging in the boundary condition that $\psi(0) = 0$. Please note that ζ in Eq. (16) is a dummy variable instead of the coordinate component.

The calculation of the energy barrier, U_{barr}, between the HCM bi-states, however, is impossible because the energy barrier is path-dependent. Considering the "kinked-to-straight" assumption, we can approximately take U_{barr} as the energy difference between the third mode shape and the first mode shape of the HCM ribbon:

$$U_{barr} = U_{3rd} - U_{1st} \tag{17}$$

if we compare the ribbon snapping to the snapping of a fixed-fixed (having fixed connections on both ends) beam. The second mode shape is omitted due to the symmetric plane at $z = 0$ of the HCM. This analogy can be inferred by the profile evolution of the centralized out-of-plane angular displacement $\psi' = \psi - \psi|_{z=\pm l}$ in Fig. 4G. The upper half of Fig. 4G is the schematic of a fixed-fixed beam deforming from its first mode shape into its

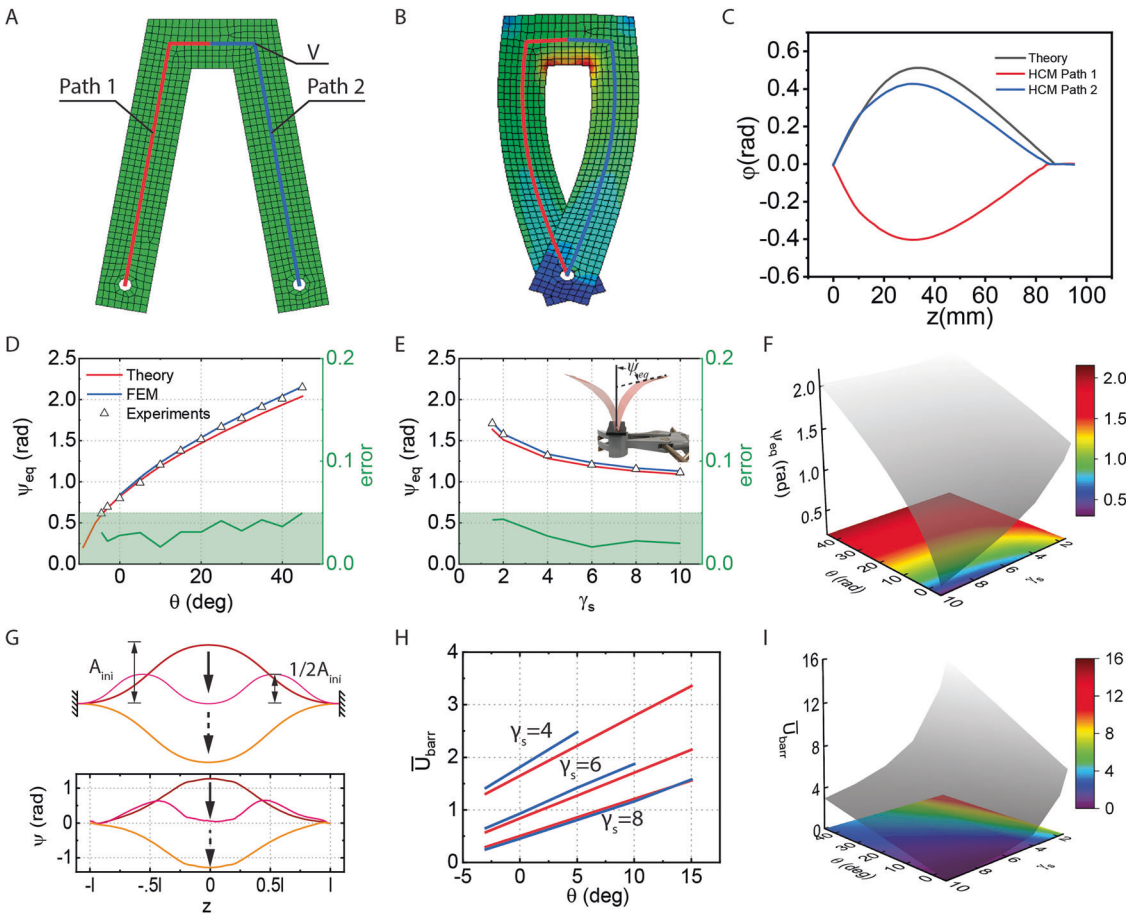


Fig. 4 | Verification of the HCM theory. A–C Comparison of rotational angles φ between Eq. (9) and the FE results calculated in SI. **D, E** Comparison of tip bending angle ψ_l or ψ_{eq} (inset) among Eq. (16), FE results, and experiments with varying θ ($\gamma_s = 6$) and γ_s ($\theta = 10^\circ$). Green shades are regions of 5% error. **F** Theoretical ψ_{eq} of the HCM with varying θ and γ_s. **G** Demonstration of the similarity between fixed-fixed beam snapping (top) and HCM snapping (bottom) in terms of angle ψ. A_{ini} is the maximum deflection of the first mode shape of the beam. $A_{ini}/2$ is the maximum deflection of the third mode shape, which is the critical state of the snapping of the beam. **H** Comparison of the non-dimensional energy barrier $\overline{U}_{barr}$ between theory and FE results. **I** Theoretical $\overline{U}_{barr}$ of the HCM with varying θ and γ_s.

third mode shape, and the bottom half is the simulated result to verify this resemblance with the HCM's geometry of $\theta = 10^{\circ}$, $\gamma_s = 6$.

Meanwhile, it is easy to know from the same total length of 2 l and the similar functions of the first and third mode shapes that

$$U_{3rd} = 4U_{1st} \tag{18}$$

Plugging in Eq. (14), the energy barrier

$$U_{barr} = 3U_{1st} = 3P_{cr} \cdot L_2\left(\sin^{-1}\frac{1}{\gamma_s} + \theta\right) \tag{19}$$

A MATLAB live script file, including the above calculations, is provided in the supplementary information (SI) to demonstrate the design process and to promote its future usage.

FE and experimental verification

Equations (9) and (16) indicate that the configuration of the assembled ribbon's midline, i.e., the values of $\varphi(s = l - z)$ at stable states, ψ_{eq} or $\psi(l)$ at stable states, is irrelevant to the material modulus E, thickness t, or ribbon width h, and is determined by the unitless shape factors θ (Fig. 1A) and $\gamma_s = L_2 / L_1$, if only the slender beam criterion of $h > 10t$ is met[32]. This conclusion offers convenience when we scale up HCMs for larger applications. If we consider the non-dimensional energy barrier $\overline{U}_{barr} = U_{barr}L_1/EI_{\eta}$ instead of the absolute energy barrier U_{barr}, the same conclusion can be drawn that it is only affected by θ and γ_s.

Thus, the verification of the above calculation is done by comparing Eqs. (9), (16), and non-dimensionalized Eq. (19) to FE and experimental results with varying θ and γ_s, as shown in Fig. 4. The theoretical rotation angle φ is calculated using MATLAB. We reproduced the assembly and snap-through process in the FE software ABAQUS/Standard for an HCM with shape factor $\theta = 10^{\circ}$, $\gamma_s = 6$, and other parameters h / L_1 = 15 mm / 12.5 mm and t / L_1 = 0.381 mm / 12.5 mm. The simulation uses 756 shell elements S4R, and the material is assumed to be linear elastic with Young's modulus E of 2 GPa and Poisson ratio v of 0.3. The experimental results of ψ_{eq} are measured with a 1-axis soft flex sensor (Bend Labs Inc.) connected to a SparkFun Pro nRF52840 Mini microcontroller.

Results in Fig. 4C show a fair agreement of the rotational angles $\varphi(s)$ between the theory Eq. (9) and the FE results, despite the assumptions. The theoretical solution Eq. (16), or ψ_{eq}, gives an error of around 5% (Fig. 4D, E) compared to the experimental measurements with varying θ and γ_s. The energy barrier can be estimated with FE simulation by taking the minimum of a series of trials with different loading conditions (Movie S6). When compared to the FE method, Eq. (19) gives a maximum error of approximately 10% (Fig. 4H). Despite the good verification results, we should be aware that this theory is still qualitative.

Using HCM for repetitive propulsion

The bistable HCM can be conveniently fabricated with tensile-resistant 2D materials like carbon fiber/epoxy, metal, plastic, and paper sheets and assembled with a pin rivet. These materials are usually too high in modulus for compliant mechanisms since their moduli are in the range of $10^9 \sim 10^{11}$ Pa and are much stronger than elastomers. However, their 2D forms will have out-of-plane stiffnesses smaller than their membrane stiffnesses by an order of $10^5 \sim 10^6$, enabling them to deform with moderate load.

On the other hand, repetitive actuation can cause the material of HCMs to develop fissures and eventually break, as discussed in our previous work.[8] It is indicated that the critical cycles of plastic HCM under repetitive actuation are logarithmically proportional to the reciprocal of ribbon thickness. And the shim plastic of 0.381 mm in thickness will have a critical cycle of $\sim 2 \times 10^4$.

Due to the "kinked-to-straight" assumption, the time scale of an HCM snapping can be analogous to that of a straight beam in compressive buckling[33]

$$t_* \approx \frac{(2l)^2}{t\sqrt{E/\rho_s}} \tag{20}$$

where ρ_s is the density of the material and t is the thickness of the ribbon. The difference in timescales of HCM snapping is shown with different materials in Fig. 1F and Movie S2. For plastic and steel HCMs with a configuration in Figs. 1 and 3, the snapping timescales are ~ 40 ms and ~16 ms from the video frames, respectively. The corresponding solutions from Eq. (20) are 68 ms and 24 ms, offering a correct order of magnitude, which can be used to estimate the critical frequency (maximum working frequency) of the HCM robots. The snapping of these plastic and steel HCMs features a clear snap sound, which is a shock wave (Movie S2). The steel HCM snaps with a swinging angular velocity of $\sim 14 \times 10^3$ °/s from the video, which is comparable to those of the throws of a professional baseball player of ~ 9000 °/s[34] and much faster than the tail beats of fish, which are about 10 Hz.

Results

Tethered pneumatic HCM fish robot

Inspired by the resemblance of HCM snapping and fish undulation, we use HCMs for fish robotic propulsion in this section. With pneumatic bending actuators[35], we made a pressure-driven HCM fish with dimensions of length × width × height = 18.6 × 6.5 × 5.2 cm^3 and a weight of 42.5 g (Fig. 5). It comprises a PETG plastic HCM body (pink, film thickness t_1 = 0.381 mm, SI), a riveted fishtail (gray, film thickness t_2 = 0.191 mm), and a hollow 3D-printed fish head with ballast. The HCM used in the fish has a geometry of $2l$ = 175 mm, $\theta = -3°$, and $\gamma_s = 6$, which yields a tip bending angle of $\psi_l = 39°$ and snapping time of ~68 ms from the theory. A pair of pneumatic bending actuators is antagonistically attached to the HCM body. When gas is pumped into these actuators, their bending deformation will snap the HCM. An alternate actuation pattern of the actuators drives the HCM fish forward. The fabrication of pneumatic actuators is similar to that in the relevant literature[24,36]. On the other hand, the reference fish robot in Fig. 5B bottom has the same dimensions of length × width × height = 18.6 × 6.5 × 5.2 cm^3 and a similar weight of ~41.6 g. It is made up of a long trapezoidal piece of plastic sheet sandwiched by two identical pneumatic bending actuators. Please note that the actuators are horizontally stuck to the plastic, while the actuators of the HCM are vertical. This leads to the difference in the bending mode, since the vertical layout generates more bionic undulation traveling from head to tail, while the horizontal layout generates more rigid swinging.

The pneumatic HCM fish swims underwater at an average horizontal speed of 1.40 BL/s or 26.54 cm/s (calculated from photo sequence) with an actuation pressure of 150 kPa and a frequency of 1.3 Hz (period = 760 ms, 39% duty cycle). In comparison, the mono-stable reference swimmer, with the same weight (~ 41.6 g) and actuation condition, swims at 0.69 BL/s or 13.10 cm/s (Fig. 5B and Movie S3), half the speed of the HCM snapping one. However, the comparison is not a perfect match due to the aforementioned geometric difference between the robots.

Figure 5C depicts the peduncle swinging angle (tip bending angle ψ_l of the HCM) of the two fishes, measured from high-fps videos (Movie S4). The two fish robots have similar undulation amplitudes, which are marked as red and blue, respectively. The HCM fish shows a novel nonlinear undulation pattern, while the reference generates the typical sinusoidal/triangular swinging. It is evident from the videos that the HCM swinging pattern gains more thrust than the reference. This interesting effect is probably due to the difference in the swinging speed of the two robots. The HCM fish flaps its tail at ~1200 °/s (consider only the time and motion from a peak to a rest state in Fig. 5C), about three times the speed of the reference one of 340 °/s, and the "squared rule" between water and velocity, i.e., $F_{\mathrm{D}} \propto v^2$, makes the HCM swimming more efficient. Detailed explanations and verification, however, will require further investigation.

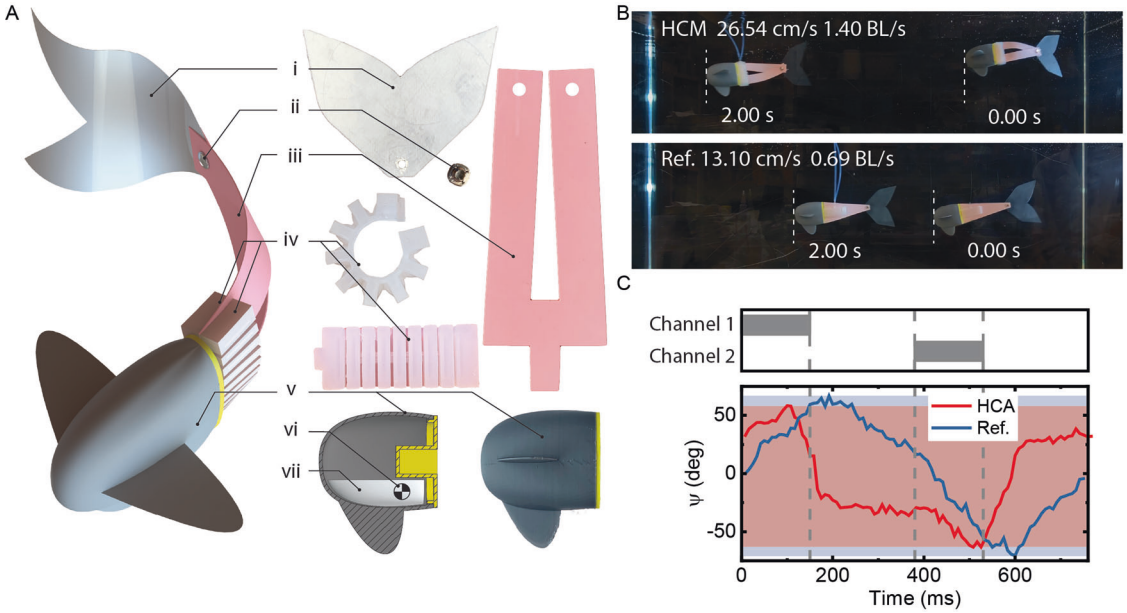


Fig. 5 | Pneumatic HCM fish robot and its comparison with the reference. A Parts and assembly of the HCM fish. i. Caudal fin ($t = 0.191$ mm), ii. Rivet pin, iii. HCM plate ($2\,l = 175$ mm, $t = 0.381$ mm, $\theta = -3°$, and $\gamma_s = 6$), iv. Pneumatic bending units, v. 3D-printed fish head, vi. position of the mass center, and vii. Cast ballast. **B** Comparison of swimming speed between the HCM and the mono-stable fish robots. Scale bar = 15 cm. **C** The recorded tail swinging angle ψ_l of the two robots. Both are actuated with 150 kPa and 1.3 Hz with a 39% duty cycle. The red and blue shades mark the amplitude of the two robots.

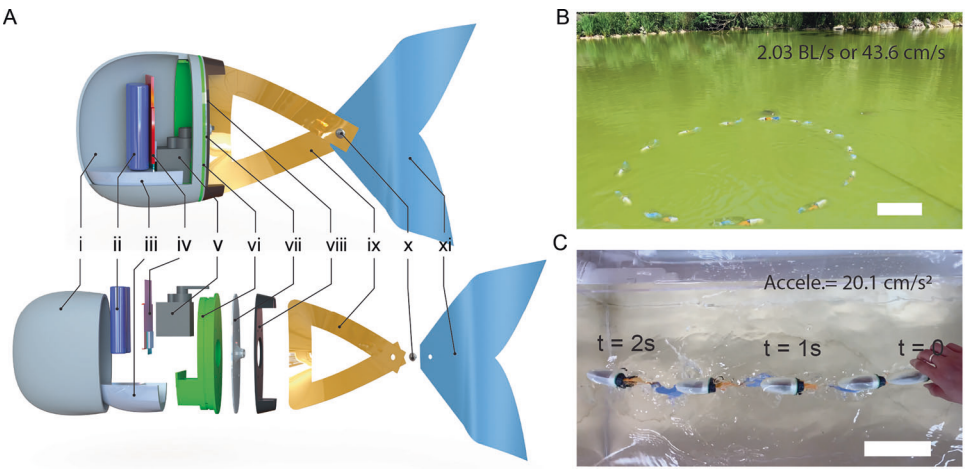


Fig. 6 | Untethered servo-driven HCM fish robot. A Assembly of the robot. i. 3D-printed fish head, ii. Battery pack (7.4 V, 350 mAh, 2-in-1 pack), iii. Cast ballast, iv. BLE microcontroller, v. Mini servo, vi. Servo holder, vii. Silicone layer, viii. Connection layer, ix. HCM plate ($t = 0.762$, $\theta = -23.5°$, $\gamma_s = 2$, and $\psi_l = 34°$), x. Pin rivet, and xi. Caudal fin ($t = 0.127$ mm). **B** Video series where the robot reaches a speed of 2.03 BL/s or 43.6 cm/s under 3 Hz swinging. The circular cruising path is for better filming. Scale bar = 20 cm. **C** The robot gives an average acceleration of 20.1 cm/s^2 during a straight dash under 3 Hz swinging. Scale bars = 15 cm.

The relation between speed and undulation frequency is hard to characterize due to the tank size and poor maneuverability of these open-loop robots. The critical pressure needed to snap the HCM in a quasi-static situation is shown in Fig. S5 (letter "S" means from the SI). An increasing θ leads to a higher energy barrier and thus a critical pressure. Simulations of the assembly and the snapping of HCMs are shown in Movie S6.

Untethered servo-driven HCM fish robot

Untethered robots usually provide more convincing evidence. With a similar design to the pneumatic HCM fish, we built an untethered servo-driven fish robot that is length × width × height = 21.5 × 4.5 × 12.0 cm^3 in size and 125 g in weight (Fig. 6A and Fig. S3). The robot is made of a PETG plastic HCM body (coral colored, film thickness $t_1 = 0.762$ mm, SI), a riveted fishtail (blue, film thickness $t_2 = 0.127$ mm), and a 3D-printed fish head. The head is 3D-printed to accommodate a 7.4 V battery set, a BLE micro-controller, and a servo motor. The HCM has a geometry of $2\,l = 174$ mm, $\gamma_s = 2$, and $\theta = -23.5°$, which gives a theoretical tip undulation amplitude of $2\psi_l = 68°$ by Eq. (16). The central point of the HCM ribbon is driven by the servo horn (part v) passing through the waterproof layer (part vi) made of silicone rubber. Simple open-loop control is used to locomote and navigate the fish (Movie S7). We made the fish density slightly smaller than the water so it could float close to the surface to receive wireless signals. The circular swimming path is fine-tuned through weight asymmetry for better filming and speed calculation. The HCM fish robot attracts local aquatic creatures to chase and then scares them away upon contact, which is an interesting phenomenon.

As a result, the fish swam 554 cm in 12.7 s, equal to an average speed of 2.03 BL/s or 43.6 cm/s under 3 Hz (6 snapping per second) swinging (Fig. 6B). A detailed speed profile is given in Fig. S3C. Figure 6C and Movie S8 show the straight dash of the fish robot with an average acceleration of about 20.1 cm/s^2 (Fig. S3D). Thrust and power consumption across frequencies (0.5–5.0 Hz) were measured using an Arduino-based setup (Fig. S4). At 3.5 Hz, the servo-driven HCM fish achieved a peak thrust of 250.31 mN; while at 3.0 Hz, it worked in optimal states, reaching a thrust of 245.66 mN

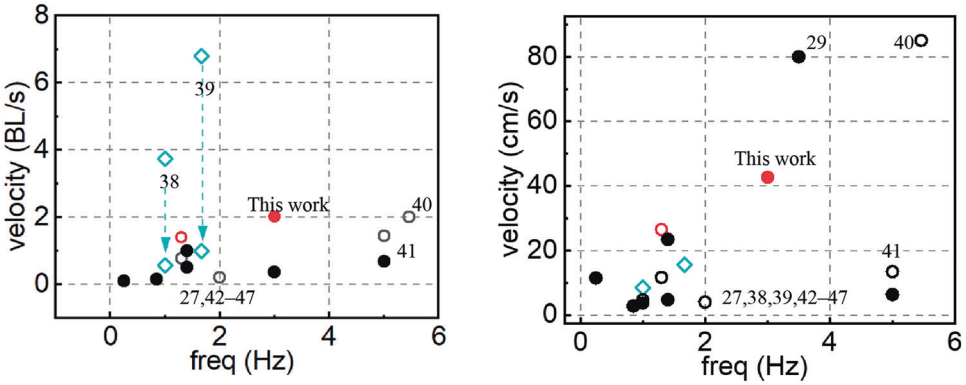


Fig. 7 | Comparison of velocity w.r.t. actuation frequency among the reported soft robotic swimmers. Hollow circles in the figure denote tethered swimmers, and solid circles denote untethered swimmers. The red-colored symbols are fish robots in this work. The blue symbols are the speed of the literature[38,39] before and after the adjustment of the criterion.

Table 1 | Comparison among multiple swimmers

Swimmers	Actuator	Key Metrics	Value	Thrust (mN)
Wang et al.[41]	DEA	Speed	7.6 cm/s (0.76 BL/s)	14
Liu et al.[42]	Servo	Speed, CoT	1.12 BL/s (0.56 m/s), 1.24	--
Hartmann et al.[43]	DEA	Speed, Power	5.1 cm/s (1.13BL/s), 35 mW	1.6
Soto et al.[44]	HASEL	Speed	13.7 cm/s (0.39 BL/s)	5.0 - 7.9
Zhang et al.[45]	DEA	Speed	111.2 mm/s (2.22 BL/s)	Low
Shen et al.[46]	IPMC	efficiency	0.24%	9.5
Chao et al.[29]	Servo	Speed	0.8 m/s (1.45 BL/s)	--
Bedenik et al.[47]	SMA	Peak speed	158 mm/s	5590
Bartlett et al.[40]	LM	Speed	2.8 cm/s (0.16 BL/s)	Low
Wang et al.[48]	Pneumatic	Speed	4.7 cm/s (0.32 BL/s)	--
Qing et al.[39]	Pneumatic	Speed, CoT	15.64 cm/s (0.87 BL/s), 11.1	70
Chi et al.[38]	Pneumatic	Speed	8.52 cm/s (0.57 BL/s)	--
This work	Servo	CoT, efficiency	5.14, 3.89% (or 79.46mN/W)	245.66

DEA dielectric elastomer actuator, *HASEL* hydraulically amplified self-healing electrostatic, *IPMC* ionic polymer–metal composites, *SMA* shape-memory alloy ape, *LM* liquid metal, *CoT* cost of transport.

and yielding a CoT (Cost of Transport) of 5.14, energy efficiency of 3.89%, and a thrust-to-power ratio of 79.46 mN/W (SI). More air undulation movies under different frequencies are provided in movie S9.

Comparisons

A comparison of the speed and the frequency of soft fish robots is shown in Fig. 7. The hollow circles in the figure are for tethered swimmers, and the solid circles are for untethered ones. Despite the onboard electronics and batteries, the untethered servo-driven fish robot in this study has a higher speed than the tethered one. If considering only untethered soft fish robots, the servo-driven HCM swimmer in this work would present a competitive speed in BL/s, better than the previous record of 1.45 BL/s by 40%[29]. Some traditional robotic fish can reach higher speeds by undulating at a high frequency (~ 10 Hz)[26,37]. Compared to them, the HCM fish have more bionic undulation with a single servo. A more comprehensive assessment of multiple swimmers[29,38,39,40,41–48], is given in Table 1.

In a similar work, Chi et al.[38] reported a speed of 3.74 BL/s (85.27 mm/s) and later Qing et al.[39] a speed of 6.8 BL/s (156.4 mm/s) for a ray-fish swimmer utilizing a bistable mechanism for aquatic propulsion[40,49–55]. These values are based on the length of the silicone pneumatic actuator. If the speed is instead calculated using the largest dimension of the ray-fish robot (~15 cm) as the body length, the corresponding values would be approximately 0.57 BL/s and 1.0 BL/s, respectively, as illustrated in Fig. 7. This highlights the impact of body length definition on reported swimming speeds. Besides, there are significant differences in the geometry of the bistable mechanisms: Chi et al. and Qing et al. used two straight ribbons and a pair of elastomeric actuators to form the prestressed and bistable structure while we used a continuous ribbon, due to which the theoretical solutions of HCM can be derived; meanwhile, the two reference papers used fixed connection at the tips of the ribbons while we used hinged connection, which lowers the energy barrier between the states and reduces the stress concentration effect around the connection.

Discussion

Bistable mechanisms are getting significant attention in the fields of soft robotics and deployable structures. Our work advances this innovation by providing analytical solutions, finite-element verification, and experimental validation for the bistable mechanism that we term HCM, demonstrating its potential to enhance robotic speed and enable untethered soft robot designs. We showcase the practical applications of HCMs with two fish robots: a pneumatic HCM fish robot, which demonstrates that the nonlinear undulation pattern resulting from bistability outperforms traditional fish robot undulation, and an untethered servo-driven swimmer with an HCM body, which was fabricated and field-tested, achieving a velocity of 2.03 BL/s or 43.6 cm/s, thrust of 245.66 mN, cost of transport (CoT) of 5.14, energy efficiency of 3.89%, and thrust-to-power ratio of 79.46 mN/W at 3 Hz undulation. These metrics position it among the fastest soft fish robots to date. The simplicity and versatility of HCMs encourage further exploration of bistable mechanisms for innovative robotic structures and applications.

Data availability

All data are available in the manuscript or in the SI.

Code availability

All data generated or used during the study appear in the submitted manuscript or in the SI.

Received: 4 March 2025; Accepted: 4 September 2025;
Published online: 09 January 2026

References

1. Chi, Y. et al. Bistable and multistable actuators for soft robots: structures, materials, and functionalities. *Adv. Mater.* **34**, 2110384 (2022).
2. Howell, L. L. Compliant Mechanisms. in *21st Century Kinematics* (ed McCarthy, J. M.) 189–216 (Springer London, London, 2013). https://doi.org/10.1007/978-1-4471-4510-3_7.
3. Daynes, S., Potter, K. D. & Weaver, P. M. Bistable prestressed buckled laminates. *Compos. Sci. Technol.* **68**, 3431–3437 (2008).
4. Kebadze, E., Guest, S. D. & Pellegrino, S. Bistable prestressed shell structures. *Int. J. Solids Struct.* **41**, 2801–2820 (2004).
5. Daynes, S. & Weaver, P. M. Stiffness tailoring using prestress in adaptive composite structures. *Compos. Struct.* **106**, 282–287 (2013).
6. Bilanin, Alan J. & Robert M. McKillip Jr. Actuating device with at least three stable positions. United States Patent US6345792B2, filed March 9, 2001, and issued February 12, 2002. https://patents.google.com/patent/US6345792B2/en.
7. Xiong, Z., Su, Y. & Lipson, H. Fast Untethered Soft Robotic Crawler with Elastic Instability. in *2023 IEEE International Conference on Robotics and Automation (ICRA)* 2606–2612 https://doi.org/10.1109/ICRA48891.2023.10160610 (2023).
8. Xiong, Z. et al. Rapid grasping of fabric using bionic soft grippers with elastic instability. in *2023 IEEE/RSJ International Conference on Intelligent Robots and Systems (IROS)* 6449–6455 https://doi.org/10.1109/IROS55552.2023.10341428 (2023).
9. Bambrick, T., Viquerat, A. & Siddall, R. Does bistability improve swimming performance in robotic fish? *Adv. Intell. Syst.* **6**, 2300748 (2024).
10. Longo, S. J. et al. Beyond power amplification: latch-mediated spring actuation is an emerging framework for the study of diverse elastic systems. *J. Exp. Biol.* **222**, jeb197889 (2019).
11. Deegan, R. D. Finessing the fracture energy barrier in ballistic seed dispersal. *PNAS* **109**, 5166–5169 (2012).
12. Taylor, P. E., Card, G., House, J., Dickinson, M. H. & Flagan, R. C. High-speed pollen release in the white mulberry tree, Morus alba L. *Sex. Plant Reprod.* **19**, 19–24 (2006).
13. Forterre, Y., Skotheim, J. M., Dumais, J. & Mahadevan, L. How the Venus flytrap snaps. *Nature* **433**, 421–425 (2005).
14. Smith, M. L., Yanega, G. M. & Ruina, A. Elastic instability model of rapid beak closure in hummingbirds. *J. Theor. Biol.* **282**, 41–51 (2011).
15. Patek, S. N., Baio, J. E., Fisher, B. L. & Suarez, A. V. Multifunctionality and mechanical origins: Ballistic jaw propulsion in trap-jaw ants. *Proc. Natl. Acad. Sci. USA* **103**, 12787–12792 (2006).
16. Faber, J. A., Arrieta, A. F. & Studart, A. R. Bioinspired spring origami. *Science* **359**, 1386–1391 (2018).
17. Rus, D. & Tolley, M. T. Design, fabrication and control of soft robots. *Nature* **521**, 467–475 (2015).
18. Miao, J. & Sun, S. Design, actuation, and functionalization of untethered soft magnetic robots with life-like motions: a review. *J. Magn. Magn. Mater.* **586**, 171160 (2023).
19. Shepherd, R. F. et al. Using explosions to power a soft robot. *Angew. Chem. Int. Ed.* **52**, 2892–2896 (2013).
20. Bartlett, N. W. et al. A 3D-printed, functionally graded soft robot powered by combustion. *Science* **349**, 161–165 (2015).
21. Tolley, M. T. et al. An untethered jumping soft robot. in *2014 IEEE/RSJ International Conference on Intelligent Robots and Systems* 561–566 https://doi.org/10.1109/IROS.2014.6942615 (2014).
22. Keithly, D. et al. A cephalopod-inspired combustion powered hydro-jet engine using soft actuators. *Extrem. Mech. Lett.* **20**, 1–8 (2018).
23. Aubin, C. A. et al. Powerful, soft combustion actuators for insect-scale robots. *Science* **381**, 1212–1217 (2023).
24. Mosadegh, B. et al. Pneumatic networks for soft robotics that actuate rapidly. *Adv. Funct. Mater.* **24**, 2163–2170 (2014).
25. Marchese, A. D., Onal, C. D. & Rus, D. Autonomous soft robotic fish capable of escape maneuvers using fluidic elastomer actuators. *Soft Robot.* **1**, 75–87 (2014).
26. Iguchi, K. et al. Agile robotic fish based on direct drive of continuum body. *npj Robot* **2**, 7 (2024).
27. Tang, Y. et al. Leveraging elastic instabilities for amplified performance: spine-inspired high-speed and high-force soft robots. *Sci. Adv.* **6**, eaaz6912 (2020).
28. Tang, D. et al. Bistable soft jumper capable of fast response and high takeoff velocity. *Sci. Robot.* **9**, eadm8484 (2024).
29. Chao, X., Hameed, I., Navarro-Alarcon, D. & Jing, X. A Controllable nonlinear bistable "fishtail" boosting robotic swimmer with excellent maneuverability and high energy efficiency. *Soft Robot.* https://doi.org/10.1089/soro.2024.0038 (2024).
30. Xiong, Z., Xiao, H. & Chen, X. Fractal-inspired soft deployable structure: a theoretical study. *Soft Matter* **17**, 4834–4841 (2021).
31. Zhang, Y., Jiao, Y., Wu, J., Ma, Y. & Feng, X. Configurations evolution of a buckled ribbon in response to out-of-plane loading. *Extrem. Mech. Lett.* **34**, 100604 (2020).
32. Timoshenko, S. P. & Gere, J. M. *Theory of Elastic Stability* (Courier Corporation, 2009).
33. Gomez, M., Moulton, D. E. & Vella, D. Critical slowing down in purely elastic 'snap-through' instabilities. *Nat. Phys.* **13**, 142–145 (2017).
34. Roach, N. T., Venkadesan, M., Rainbow, M. J. & Lieberman, D. E. Elastic energy storage in the shoulder and the evolution of high-speed throwing in Homo. *Nature* **498**, 483–486 (2013).
35. Ilievski, F., Mazzeo, A. D., Shepherd, R. F., Chen, X. & Whitesides, G. M. Soft robotics for chemists. *Angew. Chem. Int. Ed.* **50**, 1890–1895 (2011).
36. Shepherd, R. F. et al. Multigait soft robot. *Proc. Natl. Acad. Sci. USA* **108**, 20400–20403 (2011).
37. Clapham, R. J. & Hu, H. iSplash-II: realizing fast carangiform swimming to outperform a real fish. in *2014 IEEE/RSJ International Conference on Intelligent Robots and Systems* 1080–1086 https://doi.org/10.1109/IROS.2014.6942692 (2024).
38. Chi, Y., Hong, Y., Zhao, Y., Li, Y. & Yin, J. Snapping for high-speed and high-efficient butterfly stroke–like soft swimmer. *Sci. Adv.* **8**, eadd3788 (2022).
39. Qing, H. et al. Spontaneous snapping-induced jet flows for fast, maneuverable surface and underwater soft flapping swimmer. *Sci. Adv.* **10**, eadq4222 (2024).
40. Bartlett, M. D. et al. High thermal conductivity in soft elastomers with elongated liquid metal inclusions. *PNAS* **114**, 2143–2148 (2017).
41. Wang, R. et al. Fast-swimming soft robotic fish actuated by bionic muscle. *Soft Robot.* **11**, 845–856 (2024).
42. Liu, S., Liu, C., Wei, G., Ren, L. & Ren, L. Design, modeling, and optimization of hydraulically powered double-joint soft robotic fish. *IEEE Trans. Robot.* **41**, 1211–1223 (2025).
43. Hartmann, F. et al. Highly agile flat swimming robot. *Sci. Robot.* **10**, eadr0721 (2025).
44. Soto, K., Hess, I., Schrader, B., He, S. & Musgrave, P. Improving swimming performance in soft robotic fish with distributed muscles and embedded kinematic sensing. in *2025 IEEE 8th International Conference on Soft Robotics (RoboSoft)* 1–6 https://doi.org/10.1109/RoboSoft63089.2025.11020876 (2025).
45. Zhang, Y. et al. A manta ray-inspired fast-swimming soft electrohydraulic robotic fish. *IEEE Robot. Autom. Lett.* **9**, 8043–8050 (2024).

46. Shen, Q., Wang, T., Wen, L., Liang, J. & Chen, Y. On the thrust efficiency of an IPMC actuated robotic swimmer: dynamic modeling and experimental investigation. https://doi.org/10.13140/RG.2.1.2418.2488 (2012).
47. Bedenik, G. et al. Bistable SMA-driven engine for pulse-jet locomotion in soft aquatic robots. in *2025 IEEE 8th International Conference on Soft Robotics (RoboSoft)* 1–8 https://doi.org/10.1109/RoboSoft63089.2025.11020924 (2025).
48. Wang, S. et al. Jellyfish-inspired soft robot driven by pneumatic bistable actuators. *Soft Robot.* https://doi.org/10.1089/soro.2023.0212 (2024).
49. van den Berg, S. C., Scharff, R. B. N., Rusák, Z. & Wu, J. Biomimetic Design of a Soft Robotic Fish for High Speed Locomotion. In *Biomimetic and Biohybrid Systems* (eds Vouloutsi, V. et al.) 366–377 (Springer International Publishing, Cham, 2020).
50. Li, T. et al. Fast-moving soft electronic fish. *Sci. Adv.* **3**, e1602045 (2017).
51. Katzschmann, R. K., DelPreto, J., MacCurdy, R. & Rus, D. Exploration of underwater life with an acoustically controlled soft robotic fish. *Sci. Robot.* **3**, eaar3449 (2018).
52. Jin, H. et al. A starfish robot based on soft and smart modular structure (SMS) actuated by SMA wires. *Bioinspir. Biomim.* **11**, 056012 (2016).
53. Song, S.-H. et al. Turtle mimetic soft robot with two swimming gaits. *Bioinspir. Biomim.* **11**, 036010 (2016).
54. Serchi, F. G., Arienti, A. & Laschi, C. Biomimetic vortex propulsion: toward the new paradigm of soft unmanned underwater vehicles. *IEEE/ASME Trans. Mechatron.* **18**, 484–493 (2013).
55. Sfakiotakis, M., Kazakidi, A., Chatzidaki, A., Evdaimon, T. & Tsakiris, D. P. Multi-arm robotic swimming with octopus-inspired compliant web. in *2014 IEEE/RSJ International Conference on Intelligent Robots and Systems* 302–308 https://doi.org/10.1109/IROS.2014.6942576 (2014).

Acknowledgements

We especially thank Yichao Tang for the help with the experiments, and Jiefeng Sun for the simulation suggestion. This work was supported by the Environment Engineering Department at Columbia University, the U.S. National Science Foundation (NSF) AI Institute for Dynamical Systems grant 2112085, and the Startup Funding from Texas State University.

Author contributions

Z.X. conceived the presented idea, developed the theory, built the simulation, designed and carried out the experiments, and composed the manuscript. S.L.W. helped with the filming tasks in Movie 1; L.C. helped carry out the experiments and collect data. H.L. supervised the project and revised the manuscript. and M.S. supported the project and helped revise the manuscript.

Competing interests

The authors declare no competing interests.

Additional information

Supplementary information The online version contains supplementary material available at https://doi.org/10.1038/s44182-025-00053-0.

Correspondence and requests for materials should be addressed to Zechen Xiong.

Reprints and permissions information is available at http://www.nature.com/reprints

Publisher's note Springer Nature remains neutral with regard to jurisdictional claims in published maps and institutional affiliations.

Open Access This article is licensed under a Creative Commons Attribution-NonCommercial-NoDerivatives 4.0 International License, which permits any non-commercial use, sharing, distribution and reproduction in any medium or format, as long as you give appropriate credit to the original author(s) and the source, provide a link to the Creative Commons licence, and indicate if you modified the licensed material. You do not have permission under this licence to share adapted material derived from this article or parts of it. The images or other third party material in this article are included in the article's Creative Commons licence, unless indicated otherwise in a credit line to the material. If material is not included in the article's Creative Commons licence and your intended use is not permitted by statutory regulation or exceeds the permitted use, you will need to obtain permission directly from the copyright holder. To view a copy of this licence, visit http://creativecommons.org/licenses/by-nc-nd/4.0/.

© The Author(s) 2025